Nanoscale

PAPER

Dendritic growth of monolayer ternary WS$_{2(1-x)}$Se$_{2x}$ flakes for enhanced hydrogen evolution reaction†

Yu Zhang,[a] Kaili Liu,[a,b] Fengmei Wang,[a,b] Tofik Ahmed Shifa,[a,b] Yao Wen,[b,c] Feng Wang,[a,b] Kai Xu,[a,b] Zhenxing Wang,[a] Chao Jiang[c] and Jun He [ID] *[a]

Two-dimensional transition-metal dichalcogenides (TMDs) have attracted much research interest in the hydrogen evolution reaction (HER) due to their superior electrocatalytic properties. Beyond binary TMDs, ternary TMD alloys, as electrocatalysts, were also gradually acknowledged for their remarkable efficiency in HER. Herein, we successfully synthesized monolayer dendritic ternary WS$_{2(1-x)}$Se$_{2x}$ flakes possessing abundant active edge sites on a single crystalline SrTiO$_3$ (STO(100)). And the obtained dendritic WS$_{2(1-x)}$Se$_{2x}$ flakes could be transferred intact to arbitrary substrates, for example, SiO$_2$/Si and Au foils. Intriguingly, the transferred dendritic WS$_{2(1-x)}$Se$_{2x}$ flakes on Au foil demonstrate a significant HER performance, reflected by a rather lower Tafel slope of ~69 mV dec^{-1} and a much higher exchange current density of ~50.1 μA cm^{-2} outshining other CVD-grown two-dimensional TMD flakes. Furthermore, our new material shows excellent stability in electro-catalyzing the HER, suggestive of its robustness for being an excellent electrocatalyst. We believe that this work broadens the outlook for the synthesis of two-dimensional TMDs toward satisfying the applications in electrocatalysis.

Introduction

Recently, two-dimensional (2D) layered transition-metal dichalcogenides (TMDs) have attracted a wide horizon of research interest due to their fascinating optical and electronic properties,[1–6] such as a tunable bandgap from indirect to direct when thinned down to a monolayer,[7,8] a tunable band structure with strain,[9] highly reactive edge sites for hydrogen evolution reaction (HER),[10] *etc*. All these properties have made TMDs widely applicable in electronics,[11] optoelectronics,[1,12] and electrocatalysis.[13–15] Hence, for realizing such applications, the synthesis of uniform monolayer TMDs with high crystal quality is an important prerequisite. Compared with numerous growth methods, including mechanical exfoliation,[16] liquid exfoliation,[17] transition metal sulfurization,[18] decomposition of thiomolybdates[19] and physical vapor deposition (PVD),[20] the chemical vapor deposition (CVD) technique has been demonstrated as the most efficient and suitable way

to achieve uniform monolayer TMDs due to its tunable parameters and growth substrates.[21–24] In fact, CVD-grown TMD triangles on different substrates have been reported meant for electronic and optoelectronic devices exhibiting excellent properties.[25–27]

Recently, CVD-grown binary TMD layers, such as MoS$_2$,[28] MoSe$_2$,[29] WS$_2$,[30] and WSe$_2$,[31] have been synthesized and applied for HER catalysis. It is well known that the edges of TMDs are considered catalytically active due to their low hydrogen binding energy (ΔGH_o).[10] Furthermore, the electrocatalytic activity for HER linearly correlates with the number of active edge sites of monolayer TMDs.[10] Then much effort has been made to improve the HER activity of TMDs through various techniques such as morphological engineering,[32–34] introducing other metal atoms (Co, Ni, Fe)[35] or non-metal atoms[36] into TMD-based electrocatalysts and phase engineering.[37] In this quest, CVD-grown vertical TMD layers,[31] small sized TMD triangles with high nucleation density[32] and dendritic TMD flakes[33] have shown enhanced HER activity owing to their geometrically exposed active edge sites. Moreover, ternary TMD alloys, such as CoS$_{2x}$Se$_{2(1-x)}$ nanowires,[38] WS$_{2(1-x)}$Se$_{2x}$ nanotubes,[39] WS$_{2(1-x)}$Se$_{2x}$ nanoribbons[40] and WS$_{2(1-x)}$Se$_{2x}$ particles,[41] synthesized on carbon fibers and Ni foam are also investigated for HER. Consequently, the ternary TMD alloys exhibit a better HER performance than their binary counterparts owing to their many more unsaturated active sites, which is induced by lattice distortion from different radii of atoms on the basal planes. However, compared with 2D binary TMD

[a]CAS Center for Excellence in Nanoscience, CAS Key Laboratory of Nanosystem and Hierarchical Fabrication National Center for Nanoscience and Technology, Beijing 100190, China. E-mail: hej@nanoctr.cn
[b]University of Chinese Academy of Science, No.19A Yuquan Road, Beijing 100049, China
[c]CAS Center for Excellence in Nanoscience, CAS Key Laboratory for Standardization and Measurement for Nanotechnology, National Center for Nanoscience and Technology, Beijing 100190, China
†Electronic supplementary information (ESI) available: SEM and OM images of dendritic WS$_{2(1-x)}$Se$_{2x}$ and WS$_2$ flakes. See DOI: 10.1039/c7nr00895c

layers, the synthesis of ternary monolayer TMD layers for HER is rare and inefficient, especially for monolayer $WS_{2(1-x)}Se_{2x}$. This is perhaps due to its stringent parameter optimization requirements for controlling the S to Se ratio at the monolayer level.

Herein, using a facile low pressure chemical vapor deposition (CVD) method, we initially present a uniform synthesis of monolayer dendritic ternary $WS_{2(1-x)}Se_{2x}$ flakes on a single crystalline $SrTiO_3$(STO(100)) substrate. The obtained dendritic $WS_{2(1-x)}Se_{2x}$ flakes, decorated with abundant edges on STO (100), can be transferred to arbitrary substrates, for example, SiO_2/Si and Au foils without any damage on the material. Notably, the transferred $WS_{2(1-x)}Se_{2x}$ flakes on Au foils served as working electrodes in a three-electrode system for catalyzing HER, exhibiting an excellent performance with a low Tafel slope and a rather high exchange current density. Most importantly, it demonstrates impressively excellent stability, suggesting a robust surface of dendritic $WS_{2(1-x)}Se_{2x}$ flakes.

Experimental section

Synthesis of dendritic $WS_{2(1-x)}Se_{2x}$ flakes and transfer

In the typical growth, a two-temperature zone chemical vapor deposition (CVD) system was used (ESI†). The dendritic $WS_{2(1-x)}Se_{2x}$ flakes were obtained by sulfurization and selenylation of WO_3 powder. Sulfur powder was placed in the upstream part of a tube outside the hot zone and mildly sublimated at ~102 °C by heating belts. And the front zone is loaded with Se powder while the WO_3 powder and STO(100) substrates are placed inside the back zone in a proper order. Ar gas (50 standard cubic centimeters per minute (sccm)) and H_2 gas (5 sccm) were used to transport WO_{3-x} vapor species to the downstream substrates. The growth pressure was pumped down to about 100 Pa all along the growth process. The growth temperature of WO_3 powder and the substrate is ~860 °C with a heating rate of 30 °C min^{-1}, and the temperature of Se powder is 250 °C at a heating rate of 10 °C min^{-1}. And the growth time is 30 minutes. The as-grown dendritic $WS_{2(1-x)}Se_{2x}$ samples were transferred onto arbitrary substrates with a commonly used method. First, poly(methyl methacrylate) (PMMA) was spin coated on $WS_{2(1-x)}Se_{2x}$/STO(100), and then the STO(100) substrates were etched with a concentrated HF solution until detaching the PMMA-capped $WS_{2(1-x)}Se_{2x}$ film from STO(100). Lastly, a clean SiO_2/Si substrate or other substrates were then used to "fish out" the PMMA-capped $WS_{2(1-x)}Se_{2x}$ film, followed by drying it on a hot-plate (100 °C for 5 min) and removing the PMMA with hot acetone (~60 °C) for 30 minutes or annealing at 350 °C for 1 h in the furnace.

Characterization

The morphologies of dendritic $WS_{2(1-x)}Se_{2x}$ and WS_2 flakes were characterized by optical microscopy (OM, Olympus BX51 M), Hitachi S-4800 scanning electron microscopy (SEM) and Tecnai F20 transmission electron microscopy (TEM). STEM-EDX elemental mapping was performed by using a Tecnai F20. The optical properties were characterized by using a confocal microscopy-based Raman spectrometer (Renishaw InVia, 532 nm excitation laser). X-ray photoelectron spectroscopy was performed on an ESCALAB 250 Xi. And the thickness of the obtained samples was characterized by atomic force microscopy (AFM, Bruker Icon).

Electrochemical measurements

Electrochemical measurements were performed in a three-electrode system at an electrochemical station (CHI 660D). Transferred dendritic $WS_{2(1-x)}Se_{2x}$ samples on Au foils served as a working electrode, employing a saturated calomel electrode (SCE) as the reference electrode and a platinum wire as the counter electrode. All the potentials were calibrated to a reversible hydrogen electrode (RHE). Linear sweep voltammetry was conducted in a 0.5 M H_2SO_4 electrolyte from −0.8 V to 0 V vs. RHE with a scan rate of 5 mV s^{-1}. And before the measurement, the electrolyte was sparged with pure N_2 (purity 99.999%) for about 30 min in order to achieve an oxygen free environment. Electrochemical impedance spectroscopy (EIS) was performed in the frequency range from 0.01 Hz to 0.5 MHz at the voltage of 0.15 V versus RHE.

Results and discussion

The monolayer dendritic $WS_{2(1-x)}Se_{2x}$ flakes with the atom ratio (S : Se) of 19 : 1 were synthesized on the STO(100) substrate by using a facile low pressure chemical vapor deposition (LPCVD) system (Fig. S1†). The schematic view in Fig. 1a depicts the related chemical reaction of $WS_{2(1-x)}Se_{2x}$ flake growth on STO(100). Briefly, WO_3 powder was partially reduced by sulfur and selenium vapor to form the volatile suboxide species WO_{3-x}, which was further sulfurized and selenized to achieve the formation of $WS_{2(1-x)}Se_{2x}$ on the STO(100) substrate. Sulfur powder was placed in the upstream part of the quartz tube and sublimated at ~102 °C by heating belts, while selenium powder was placed in the front hot zone with a temperature of about 250 °C. And WO_3 powder and substrates in the back hot zone were heated to ~860 °C. Both sulfur and selenium vapor were carried downstream by mixed carrier gas (Ar and H_2) and reacted with WO_3, finally resulting in the formation of $WS_{2(1-x)}Se_{2x}$ on STO(100). It is worth mentioning that the LPCVD system was pumped down to ~100 Pa in the whole growth process (more details are shown in the Experimental section and ESI Fig. S1†). The photograph in Fig. 1b exhibits a uniform yellow color of the STO(100) after growth, with respect to the left bare STO(100) substrate, which provides physical evidence for the fact that some sort of growth indeed took place. This is more evident from the scanning electron microscopy (SEM) image where the morphology of the as-grown $WS_{2(1-x)}Se_{2x}$ on STO(100) is clearly observed in Fig. 1c and S2.† It is apparent that the $WS_{2(1-x)}Se_{2x}$ flakes exhibit a relatively uniform thickness and distribution on STO (100). And the gray regions in Fig. S2† are considered as synthesized $WS_{2(1-x)}Se_{2x}$, while the dark regions thereabout rep-
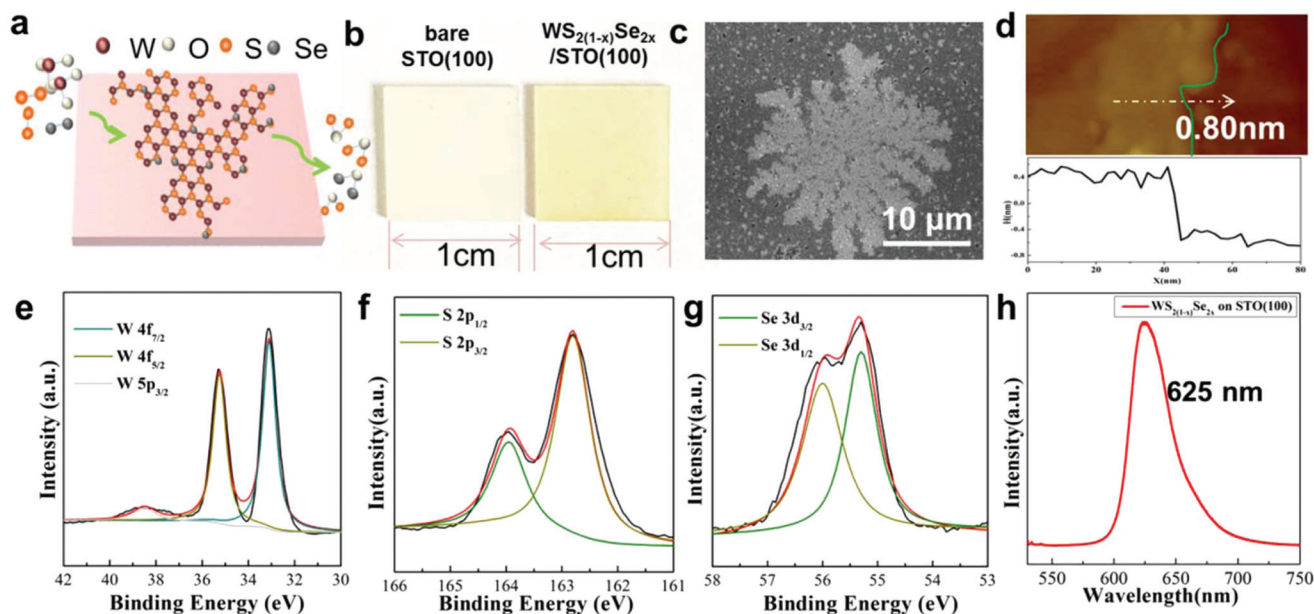
Fig. 1 LPCVD synthesis of monolayer dendritic $WS_{2(1-x)}Se_{2x}$ on the single-crystalline STO(100) substrate. (a) Schematic view presenting the surface growth of dendritic $WS_{2(1-x)}Se_{2x}$ flakes. (b) Photograph of the substrate (STO(100)) before and after the CVD growth. (c) SEM images of the as-grown dendritic ternary $WS_{2(1-x)}Se_{2x}$ flakes on STO(100). (d) AFM image and the corresponding section view along the arrow showing a monolayer flake (~0.80 nm in apparent height). High resolution XPS spectra of (e) W 4f region, (f) S 2p region, and (g) Se 3d region. (h) PL spectra of as-grown monolayer $WS_{2(1-x)}Se_{2x}$ on STO(100).

resent the bare STO(100) substrate. It is fascinating to point out that the obtained $WS_{2(1-x)}Se_{2x}$ flakes appear to have a dendritic shape with abundantly exposed curving edges. Based on our previous report,[42] this kind of unique dendritic growth of $WS_{2(1-x)}Se_{2x}$ on STO(100) should follow a diffusion-limited aggregation mechanism, which is induced by a prominent diffusion anisotropy of monomer precursors on STO(001) and the disparate lattice symmetry between $WS_{2(1-x)}Se_{2x}$ and STO(100).[42] In order to get information regarding the thickness of the flakes, we characterized our sample with respect to atomic force microscopy (AFM) and the result is depicted in Fig. 1d. The section view along the white arrow reflects an apparent height of ~0.8 nm, indicating a monolayer nature. Thus monolayer dendritic $WS_{2(1-x)}Se_{2x}$ flakes were obtained on STO(100).

Furthermore, X-ray photoelectron spectroscopy (XPS) was employed to assess the chemical states of the constituents in our synthesized $WS_{2(1-x)}Se_{2x}$, whose spectra are shown in Fig. 1e–g. From Fig. 1e, two stronger peaks at binding energies of 33.1 eV and 35.2 eV correspond to the W $4f_{7/2}$ and W $4f_{5/2}$ states, respectively. The peak at around 38.5 eV represents the W $5p_{7/2}$ state, accounting for the existence of WO_3 species due to slight surface oxidation. The chemical states of S and Se in the ternary nanoflakes can be conspicuously identified from Fig. 1f and g. The peaks at binding energies of 162.8 eV and 163.9 eV are meant for S $2p_{3/2}$ and S $2p_{1/2}$ states respectively. Moreover, Se $3d_{5/2}$ and Se $3d_{3/2}$ are substantiated from the spectra appearing at binding energies of 55.3 eV and 56.0 eV respectively. And the W and S peaks in $WS_{2(1-x)}Se_{2x}$ flakes reveal a slight shift toward lower energies compared with those in pure monolayer WS_2 flakes (see Fig. S3†), which should be

caused by the presence of Se atoms. Here, the presence of W, S and Se in the nanoflakes can be evidenced. The result of XPS can also provide valuable sources of quantitative information. Accordingly, the atomic ratio of S and Se in $WS_{2(1-x)}Se_{2x}$ is found to be close to 19 : 1 where $x \sim 0.05$. In our CVD growth, the obtained $WS_{2(1-x)}Se_{2x}$ mainly shows the S : Se ratios of about 19 : 1 under an S-saturated atmosphere, which is attributed to the stronger reducibility of S than that of Se. Collectively, the XPS data reveal the formation of ternary $WS_{2(1-x)}Se_{2x}$ flakes, which is in good agreement with previously reported values.[40,43] Besides, Raman and photoluminescence (PL) spectroscopic measurements were also performed on the as-grown $WS_{2(1-x)}Se_{2x}$ on STO(100) (with 532 nm laser excitation). Fig. 1h presents an apparent A excitonic emission located at 625.0 nm, which is in accordance with monolayer TMDs.[44] And the monolayer ternary $WS_{2(1-x)}Se_{2x}$ still maintains a direct band gap.[20] Besides, the existence of Se may induce a red shift of the PL emission peak,[25,43] which will be discussed later (Fig. 2e). The typical Raman peaks of $WS_{2(1-x)}Se_{2x}$ couldn't be observed due to being masked by the strong Raman signals of the STO(100) substrate (Fig. S4†). So the XPS data and PL spectra demonstrate the formation of monolayer ternary $WS_{2(1-x)}Se_{2x}$ alloys.

The transfer of the as-grown $WS_{2(1-x)}Se_{2x}$ from STO(100) to arbitrary substrates is necessary for illustrating their intrinsic properties, as well as for their applications. The schematic view in Fig. 2a clearly displays the fact that our transfer procedure comprises of several steps. Briefly, the transfer method is similar to the commonly used one by detaching the STO(100) substrate with a concentrated HF solution (more details
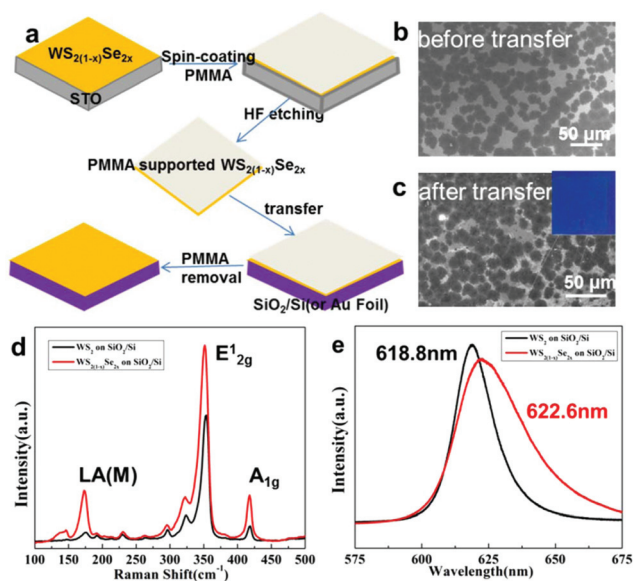
Fig. 2 Intact transference of the as-grown dendritic $WS_{2(1-x)}Se_{2x}$ flakes onto SiO_2/Si. (a) Schematic view of the whole transfer process. (b) SEM image of monolayer dendritic $WS_{2(1-x)}Se_{2x}$ flakes on STO(100). (c) SEM image of monolayer $WS_{2(1-x)}Se_{2x}$ flakes after being transferred to SiO_2/Si. (d) Raman spectra of transferred monolayer dendritic $WS_{2(1-x)}Se_{2x}$ and WS_2 flakes on SiO_2/Si. (e) PL spectra of transferred monolayer dendritic $WS_{2(1-x)}Se_{2x}$ and WS_2 flakes on SiO_2/Si.

are discussed in the Experimental section). Fig. 2b shows the SEM image of an original $WS_{2(1-x)}Se_{2x}$ sample on STO(100) with dendritic design. Using the transfer method mentioned above, the as-grown dendritic $WS_{2(1-x)}Se_{2x}$ on STO(100) can be entirely transferred to the SiO_2/Si substrate, as shown in Fig. 2c. Surprisingly, each dendritic $WS_{2(1-x)}Se_{2x}$ flake and its rough edges are still maintained, giving solid evidence of our perfect transfer. And a photograph of the transferred $WS_{2(1-x)}Se_{2x}$ on SiO_2/Si, as an inset in Fig. 2c, exhibits a uniform film, again addressing the intact transfer. For the sake of comparison and logical discussion, we synthesized monolayer dendritic WS_2 on STO(100) by the LPCVD method and followed the same transfer procedure (details of morphologies are shown in Fig. S5†). Fig. 2d and e depict the Raman and PL spectra, obtained with a 532 nm laser, of monolayer dendritics of $WS_{2(1-x)}Se_{2x}$ and WS_2 after transfer, respectively. From the Raman spectra in Fig. 2d, the pertinent peaks due to the E^1_{2g} mode (in-plane vibration), A_{1g} mode (out of plane vibration) and a second-order mode of the longitudinal acoustic phonon 2LA(M) appeared at $\sim$352 cm^{-1}, $\sim$418 cm^{-1} and $\sim$176 cm^{-1} respectively for pure and transferred WS_2 on $SiO_2/$Si. These values are in accordance with those observed for monolayer WS_2.[45] It is obvious that there exists a slight red shift in the peaks for monolayer $WS_{2(1-x)}Se_{2x}$ flakes (i.e. 350 cm^{-1} for the E^1_{2g} mode and $\sim$416 cm^{-1} for the A_{1g} mode). From the basis of reported results,[40,43] the incorporation of other atoms with different radii (Se vs. S) may cause the lattice tensile strain in the formation of $WS_{2(1-x)}Se_{2x}$, and thus induce a red shift of Raman peak positions. What's more, A_{1g}

mode and 2LA(M) mode revealed a stronger intensity compared to that of pure WS_2 (normalized by the intensity of the Si peak), which is also attributed to the Se incorporation. Fig. 2e demonstrates the room-temperature PL spectra of pure WS_2 and $WS_{2(1-x)}Se_{2x}$ after transferring them from STO(100) to $SiO_2/$Si. Interestingly, the PL peak ($\sim$622.6 nm) of $WS_{2(1-x)}Se_{2x}$ exhibits an obvious redshift compared to that of pure WS_2 ($\sim$618.8 nm). This result suggests that the presence of Se could modulate the bandgap of WS_2, along with a red shift of the PL spectrum, in agreement with published results.[38] In this case, the Raman and PL results again confirm the successful introduction of Se atoms and the formation of ternary $WS_{2(1-x)}Se_{2x}$ flakes. Moreover, the obtained dendritic $WS_{2(1-x)}Se_{2x}$ flakes can be transferred intact to arbitrary substrates, building a strong foundation for their broad applications.

In a further step, the $WS_{2(1-x)}Se_{2x}$ flakes were also transferred onto carbon-coated copper grids for transmission electron microscopy (TEM) investigations. The low-magnification TEM image in Fig. 3a shows a continuous film on the copper grids, displaying a successful transfer of our as-grown $WS_{2(1-x)}Se_{2x}$ flakes. And some obvious folding regions could be clearly distinguished around occasionally broken holes according to their different contrasts. The high-resolution transmission electron microscopy (HRTEM) image reveals a perfect hexagonal lattice, as shown in Fig. 3b. And the corresponding selective area electron diffraction (SAED) pattern (200 nm × 200 nm) shown as an inset presents only one set of diffraction spots, highly suggestive of the monolayer nature and the perfect crystal quality of our CVD synthesized $WS_{2(1-x)}Se_{2x}$
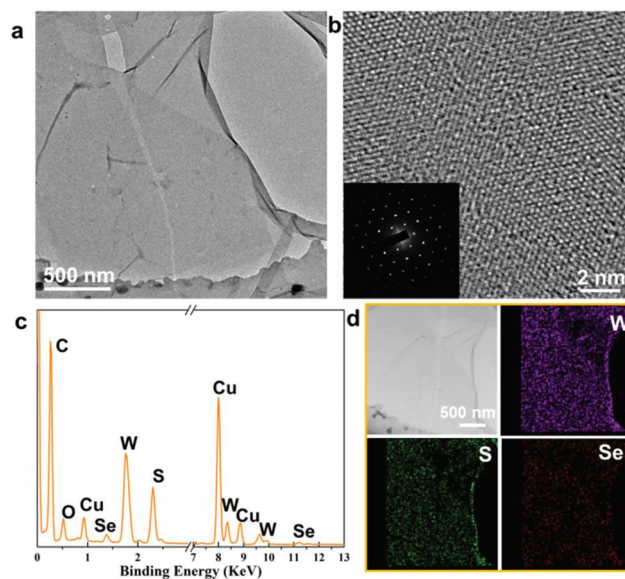

Fig. 3 High-resolution transmission electron microscopy (HRTEM) characterization of the monolayer $WS_{2(1-x)}Se_{2x}$ flakes. (a) TEM image on the edge of a broken hole of the $WS_{2(1-x)}Se_{2x}$ flakes. (b) HRTEM image of a monolayer $WS_{2(1-x)}Se_{2x}$ flake and the selective area electron diffraction (SAED) pattern as an inset. (c) EDX spectrum of the $WS_{2(1-x)}Se_{2x}$ flakes. (d) STEM-EDX elemental mapping of W, S, and Se in ternary $WS_{2(1-x)}Se_{2x}$ flakes.

flakes. Moreover, the first-order diffraction spots, corresponding to the (100) planes, demonstrate a d(100) of ~0.27 nm, which is nearly in accordance with that of monolayer WS_2.[25] The energy-dispersive X-ray (EDX) spectrum in Fig. 3c demonstrates that the $WS_{2(1-x)}Se_{2x}$ flakes consist of W, S and Se elements (other element signals come from carbon-coated copper grids), with the S : Se atomic ratio close to 19 : 1 ($x \sim 0.05$), indicating the formation of ternary $WS_{2(1-x)}Se_{2x}$ flakes. This result is in good agreement with the above XPS data. What's more, the corresponding STEM-EDX elemental mapping of W, S, and Se (Fig. 3d) suggests the uniform distribution of constituents across the $WS_{2(1-x)}Se_{2x}$ flakes, again confirming their alloy structure. Hence, the TEM images clearly prove the high quality of $WS_{2(1-x)}Se_{2x}$ flakes and their ternary alloy structure.

To evaluate the electrochemical catalytic performance, the hydrogen evolution reaction (HER) of the synthesized $WS_{2(1-x)}Se_{2x}$ flakes was investigated using a typical three electrode system in 0.5 M H_2SO_4 electrolyte (N_2 saturated) at room temperature (see the Experimental section). Firstly, monolayer $WS_{2(1-x)}Se_{2x}$ (or WS_2) flakes were transferred from STO(100) substrates to Au foils, which were used as working electrodes (Fig. S6†). Accordingly, the electrocatalytic performance was measured and linear sweep voltammetric (LSV) measurement was conducted so as to investigate the HER performances of samples under study. For comparison, the HER activities of bare Au foil and transferred dendritic WS_2 on Au foil were also measured and compared with that of dendritic $WS_{2(1-x)}Se_{2x}$. As a result, iR corrected polarization curves revealing the respective electrocatalytic performances are depicted in Fig. 4a. It is obvious that the HER performance of Au foil is very poor, suggestive of the fact that the catalytic activity observed for other samples emanates only from the grown materials. At the same current density of 10 mA cm^{-2}, the dendritic $WS_{2(1-x)}Se_{2x}$ reveals a much lower overpotential of 156 mV than that of dendritic WS_2 (~310 mV at 10 mA cm^{-2}). Hence, the polarization curves demonstrate the promotional effect of Se incorporation in $WS_{2(1-x)}Se_{2x}$ for HER performance. The Tafel slopes were extracted from the polarization curves in Fig. 4a to evaluate the efficiency of the catalysts, as shown in Fig. 4b. Similarly, the Tafel plot of monolayer dendritic $WS_{2(1-x)}Se_{2x}$ shows a noticeably lower Tafel slope of 69 mV dec^{-1} than that of dendritic WS_2 (87 mV dec^{-1}), further solidifying the promotional effect of Se in WS_2. Comparing our findings with other reported and related materials, we found that the Tafel slope of our dendritic $WS_{2(1-x)}Se_{2x}$ (69 mV dec^{-1}) is much lower than that of reported triangular $WS_{2(1-x)}Se_2$ flakes (85 mV dec^{-1}).[46] Similarly, the Tafel slope of dendritic WS_2 is calculated to be 87 mV dec^{-1}, which is also lower than that (100 mV dec^{-1}) of triangular WS_2 flakes.[30] These results suggest that the dendritic shape of $WS_{2(1-x)}Se_{2x}$ (and WS_2) flakes provides many more active edge sites than triangular flakes, thereby resulting in an improved HER performance. Therefore, the dendritic edges as well as Se incorporation of $WS_{2(1-x)}Se_{2x}$ flakes also play a significant role in the enhanced HER performance. By extrapolating the Tafel plot, the
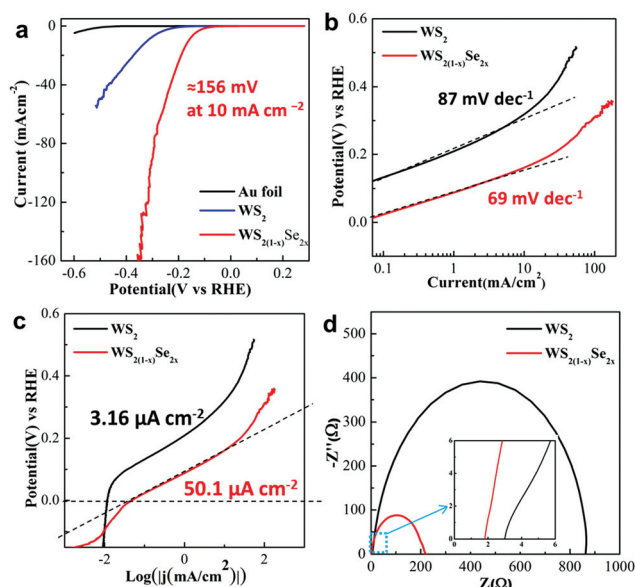

Fig. 4 HER electrocatalytic properties of bare Au foils, monolayer WS_2 and monolayer dendritic $WS_{2(1-x)}Se_{2x}$ flakes transferred onto Au foils. (a) Polarization curve of dendritic WS_2 and dendritic $WS_{2(1-x)}Se_{2x}$ on Au foils, respectively, with that of bare Au foil for comparison. (b) Corresponding Tafel plots of WS_2 and $WS_{2(1-x)}Se_{2x}$ on Au foils derived from (a). (c) Calculated exchange current densities of different samples by applying an extrapolation method to the Tafel plots. (d) Nyquist plots for WS_2 and $WS_{2(1-x)}Se_{2x}$ flakes carried out under an overpotential of −0.15 V (vs. RHE).

exchange current densities (Fig. 4c) for dendritic $WS_{2(1-x)}Se_2$ and WS_2 are found to be 50.1 μA cm^{-2} and 3.16 μA cm^{-2}, respectively. The higher exchange current density of $WS_{2(1-x)}Se_{2x}$ should be attributed to the Se-induced catalytic activity in the basal plane, which is confirmed by the increased C_{dl} value of dendritic $WS_{2(1-x)}Se_{2x}$ flakes in Fig. S7.† Additionally, electrochemical impedance spectroscopy (EIS) at 0.15 V versus RHE is employed to investigate the charge-transfer mechanism of HER. The Nyquist plots, in Fig. 4d, reveal that the charge-transfer resistances (R_{ct}) of $WS_{2(1-x)}Se_{2x}$ and WS_2 flakes are 225 Ω and 860 Ω, respectively. Besides, the series resistance (R_s) observed for $WS_{2(1-x)}Se_{2x}$ shows a rather low value of 1.8 Ω (inset plot of Fig. 4d), suggesting the small Ohmic loss between the electrolyte and the surface of the electrode. Notably, the smaller R_{ct} and R_s of dendritic $WS_{2(1-x)}Se_{2x}$ compared to that of pure WS_2 reflect the Se incorporation in $WS_{2(1-x)}Se_{2x}$ promoting a more efficient charge transfer on the surface of $WS_{2(1-x)}Se_{2x}$. Collectively, the HER tests reveal excellent electrocatalytic properties of our obtained dendritic ternary $WS_{2(1-x)}Se_{2x}$ flakes.

It's well known that the durability of a catalyst is another important aspect to evaluate its capability for realizing the long term usage. To this aim, the stability of a monolayer dendritic $WS_{2(1-x)}Se_{2x}$ electrocatalyst was tested via an accelerated disintegration test and the result is shown in Fig. 5a. After 1000 cycles of cyclic voltammetry (CV) run, there results a negligible decay in the performance of dendritic $WS_{2(1-x)}Se_{2x}$ elec-
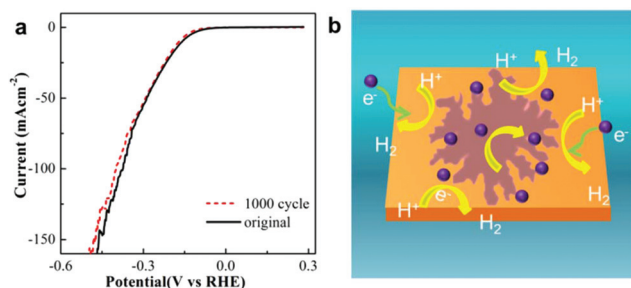
Fig. 5 Stability test and schematic view of the HER process. (a) Durability test of monolayer dendritic $WS_{2(1-x)}Se_{2x}$ catalysts. Negligible current change after 1000 cycles suggests the excellent stability of monolayer dendritic $WS_{2(1-x)}Se_{2x}$ in acid media. (b) Schematic view of dendritic $WS_{2(1-x)}Se_{2x}$ flakes operating as a HER catalyst.

trocatalysts, indicative of their excellent stability in the HER. Given the advantageous features obtained from its monolayer nature, dendritic designed flake appearance and Se incorporation, the ternary $WS_{2(1-x)}Se_{2x}$ is a better electrocatalyst in HER compared with WS_2. As a proof of concept and based on previously reported theoretical[47] and experimental results,[48] the HER activity of binary TMD flakes mainly relates to the edge density and the basal surface is thought to be catalytically inert. But, recently reported studies[40,43] proposed that the basal plane of ternary alloys (for example, $WS_{2(1-x)}Se_{2x}$) is also catalytically active. This is due to the fact that the different atomic radii of Se and S atoms may induce the crystal distortion and lattice strain on the basal plane, leading to the advent of sites convenient for catalytic activity on the basal plane.[43,46,49] Hence, a tentative schematic model in Fig. 5b provides an inference that the improved HER performance of dendritic $WS_{2(1-x)}Se_{2x}$ flakes is attributed to not only the abundant edge sites but also the active basal plane. Note that the schematic view in Fig. 5b provides only a tentative illustration, but it also gives important guidance.

Conclusions

In summary, we have achieved monolayer dendritic ternary $WS_{2(1-x)}Se_{2x}$ flakes on single crystalline STO(100) with a facile LPCVD method. The obtained dendritic $WS_{2(1-x)}Se_{2x}$ flakes decorated with abundant edge sites can be transferred intact to arbitrary substrates, such as SiO_2/Si and Au foils. Intriguingly, our synthesized monolayer dendritic $WS_{2(1-x)}Se_{2x}$ flakes on Au foil exhibit a much higher electrocatalytic activity than dendritic WS_2 flakes and the reported triangular $WS_{2(1-x)}Se_{2x}$ flakes in acid media. Notably, the dendritic shape and Se incorporation of $WS_{2(1-x)}Se_{2x}$ flakes play a significant role for the improved HER activity. The transferred $WS_{2(1-x)}Se_{2x}$ flakes on Au foil exhibit a low overpotential of ~156 mV at 10 mA cm^{-2}, a rather low Tafel slope of ~69 mV dec^{-1} and a higher exchange current density of ~50.1 µA cm^{-2}. Moreover, excellent durability suggests that the dendritic $WS_{2(1-x)}Se_{2x}$ flake is a perfect candidate for highly efficient electrocatalysis in HER.

This work will pave a new way for fabricating electrocatalysts and other electronic devices.

Acknowledgements

Notes and references

1 Q. H. Wang, K. Kalantar-Zadeh, A. Kis, J. N. Coleman and M. S. Strano, *Nat. Nanotechnol.*, 2012, **7**, 699.

2 B. Radisavljevic, A. Radenovic, J. Brivio, V. Giacometti and A. Kis, *Nat. Nanotechnol.*, 2011, **6**, 147.

3 M. Chhowalla, H. S. Shin, G. Eda, L. J. Li, K. P. Loh and H. Zhang, *Nat. Chem.*, 2013, **5**, 263.

4 A. Splendiani, L. Sun, Y. Zhang, T. Li, J. Kim, C. Y. Chim, G. Galli and F. Wang, *Nano Lett.*, 2010, **10**, 1271.

5 S. Zheng, L. Sun, X. Zhou, F. Liu, Z. Liu, Z. Shen and H. Fan, *Adv. Opt. Mater.*, 2015, **3**, 1600–1605.

6 S. Zheng, L. Sun, T. Yin, A. Dubrovkin, F. Liu, Z. Liu, Z. Shen and H. Fan, *Appl. Phys. Lett.*, 2015, **106**, 063113.

7 Y. Zhang, T. R. Chang, B. Zhou, Y. T. Cui, H. Yan, Z. Liu, F. Schmitt, J. Lee, R. Moore and Y. Chen, *Nat. Nanotechnol.*, 2014, **9**, 111.

8 K. F. Mak, C. Lee, J. Hone, J. Shan and T. F. Heinz, *Phys. Rev. Lett.*, 2010, **105**, 474.

9 H. Shi, H. Pan, Y. W. Zhang and B. I. Yakobson, *Phys. Rev. B: Condens. Matter*, 2013, **87**, 2095.

10 T. F. Jaramillo, K. P. Jørgensen, J. Bonde, J. H. Nielsen, S. Horch and I. Chorkendorff, *Science*, 2007, **317**, 100.

11 S. Wu, J. S. Ross, G. B. Liu, G. Aivazian, A. Jones, Z. Fei, W. Zhu, D. Xiao, W. Yao and D. Cobden, *Nat. Phys.*, 2013, **9**, 1.

12 L. Britnell, R. M. Ribeiro, A. Eckmann, R. Jalil, B. D. Belle, A. Mishchenko, Y. J. Kim, R. V. Gorbachev, T. Georgiou and S. V. Morozov, *Science*, 2013, **340**, 1311.

13 J. Kibsgaard, Z. Chen, B. N. Reinecke and T. F. Jaramillo, *Nat. Mater.*, 2012, **11**, 963.

14 J. Xie, H. Zhang, S. Li, R. Wang, X. Sun, M. Zhou, J. Zhou, X. W. Lou and Y. Xie, *Adv. Mater.*, 2013, **25**, 5807.

15 Y. H. Chang, C. T. Lin, T. Y. Chen, C. L. Hsu, Y. H. Lee, W. Zhang, K. H. Wei and L. J. Li, *Adv. Mater.*, 2013, **25**, 756.

16 S. G. Benka, *Proc. Natl. Acad. Sci. U. S. A.*, 2005, **102**, 10451.

17 J. N. Coleman, M. Lotya, A. O'Neill, S. D. Bergin, P. J. King, U. Khan, K. Young, A. Gaucher, S. De and R. J. Smith, *Science*, 2011, **331**, 568.

18 Y. Shi, W. Zhou, A. Y. Lu, W. Fang, Y. H. Lee, A. L. Hsu, S. M. Kim, K. K. Kim, H. Y. Yang and L. J. Li, *Nano Lett.*, 2012, **12**, 2784.

19 K. K. Liu, W. Zhang, Y. H. Lee, Y. C. Lin, M. T. Chang, C. Y. Su, C. S. Chang, H. Li, Y. Shi and H. Zhang, *Nano Lett.*, 2012, **12**, 1538.

20 Q. Feng, Y. Zhu, J. Hong, M. Zhang, W. Duan, N. Mao, J. Wu, H. Xu, F. Dong and F. Lin, *Adv. Mater.*, 2014, **26**, 2648.

21 Y. H. Lee, X. Q. Zhang, W. Zhang, M. T. Chang, C. T. Lin, K. D. Chang, Y. C. Yu, J. T. Wang, C. S. Chang and L. J. Li, *Adv. Mater.*, 2012, **24**, 2320.

22 S. Najmaei, Z. Liu, W. Zhou, X. Zou, G. Shi, S. Lei, B. I. Yakobson, J. C. Idrobo, P. M. Ajayan and J. Lou, *Nat. Mater.*, 2013, **12**, 754.

23 A. M. V. D. Zande, P. Y. Huang, D. A. Chenet, T. C. Berkelbach, Y. M. You, G. H. Lee, T. F. Heinz, D. R. Reichman, D. A. Muller and J. C. Hone, *Nat. Mater.*, 2013, **12**, 554.

24 Q. Ji, Y. Zhang, T. Gao, Y. Zhang, D. Ma, M. Liu, Y. Chen, X. Qiao, P. H. Tan and M. Kan, *Nano Lett.*, 2013, **13**, 3870.

25 Y. Zhang, Y. Zhang, Q. Ji, J. Ju, H. Yuan, J. Shi, T. Gao, D. Ma, M. Liu and Y. Chen, *ACS Nano*, 2013, **7**, 8963.

26 W. Zhang, J. K. Huang, C. H. Chen, Y. H. Chang, Y. J. Cheng and L. J. Li, *Adv. Mater.*, 2013, **25**, 3456.

27 J. K. Huang, J. Pu, C. L. Hsu, M. H. Chiu, Z. Y. Juang, Y. H. Chang, W. H. Chang, Y. Iwasa, T. Takenobu and L. J. Li, *ACS Nano*, 2014, **8**, 923.

28 J. V. Lauritsen, J. Kibsgaard and S. Helveg, *Nat. Nanotechnol.*, 2007, **2**, 53.

29 D. Kong, H. Wang, J. J. Cha, M. Pasta, K. J. Koski, J. Yao and Y. Cui, *Nano Lett.*, 2013, **13**, 1341.

30 Y. Zhang, J. Shi, G. Han, M. Li, Q. Ji, D. Ma, Y. Zhang, C. Li, X. Lang and Y. Zhang, *Nano Res.*, 2015, **8**, 2881.

31 H. Wang, D. Kong, P. Johanes, J. J. Cha, G. Zheng, K. Yan, N. Liu and Y. Cui, *Nano Lett.*, 2013, **13**, 3426.

32 J. Shi, D. Ma, G. F. Han, Y. Zhang, Q. Ji, T. Gao, J. Sun, X. Song, C. Li and Y. Zhang, *ACS Nano*, 2014, **8**, 10196.

33 Y. Zhang, Q. Ji, G. F. Han, J. Ju, J. Shi, D. Ma, J. Sun, Y. Zhang, M. Li and X. Y. Lang, *ACS Nano*, 2014, **8**, 8617.

34 Y. Zhang, B. Ouyang, J. Xu, S. Chen, R. Rawat and H. Fan, *Adv. Energy Mater.*, 2016, **6**, 1600221.

35 D. Merki, H. Vrubel, L. Rovelli, S. Fierro and X. Hu, *Chem. Sci.*, 2012, **3**, 2515.

36 C. Sun, J. Zhang, J. Ma, P. Liu, D. Gao, K. Tao and D. Xue, *J. Mater. Chem. A*, 2016, **4**, 11234.

37 M. A. Lukowski, A. S. Daniel, F. Meng, A. Forticaux, L. Li and S. Jin, *J. Am. Chem. Soc.*, 2013, **135**, 10274.

38 K. Liu, F. Wang, K. Xu, T. A. Shifa, Z. Cheng, X. Zhan and J. He, *Nanoscale*, 2016, **8**, 4699.

39 K. Xu, F. Wang, Z. Wang, X. Zhan, Q. Wang, Z. Cheng, M. Safdar and J. He, *ACS Nano*, 2014, **8**, 8468.

40 F. Wang, J. Li, F. Wang, T. A. Shifa, Z. Cheng, Z. Wang, K. Xu, X. Zhan, Q. Wang, Y. Huang and J. He, *Adv. Funct. Mater.*, 2015, **25**, 6077.

41 H. Zhou, F. Yu, J. Sun, H. Zhu, I. K. Mishra, S. Chen and Z. Ren, *Nano Lett.*, 2016, **16**, 7604.

42 Y. Zhang, Q. Ji, J. Wen, J. Li, C. Li, J. Shi, X. Zhou, K. Shi, H. Chen and Y. Li, *Adv. Funct. Mater.*, 2016, **26**, 3299.

43 Q. Fu, L. Yang, W. Wang, A. Han, J. Huang, P. Du, Z. Fan, J. Zhang and B. Xiang, *Adv. Mater.*, 2015, **27**, 4732.

44 H. R. Gutiérrez, N. Perea-López, A. L. Elías, A. Berkdemir, B. Wang, R. Lv, F. López-Urías, V. H. Crespi, H. Terrones and M. Terrones, *Nano Lett.*, 2013, **13**, 3447.

45 A. Berkdemir, H. R. Gutiérrez, A. R. Botelloméndez, N. Perealópez, A. L. Elías, C. Chia, B. Wang, V. H. Crespi, F. Lópezurías and J. Charlier, *Sci. Rep.*, 2013, **3**, 1755.

46 J. Xie, J. Zhang, S. Li, F. Grote, X. Zhang, H. Zhang, R. Wang, Y. Lei, B. Pan and Y. Xie, *J. Am. Chem. Soc.*, 2013, **135**, 17881.

47 A. M. Appel, D. L. Dubois and M. R. Dubois, *J. Am. Chem. Soc.*, 2005, **127**, 12717.

48 J. Bonde, P. G. Moses, T. F. Jaramillo, J. K. Nørskov and I. Chorkendorff, *Faraday Discuss.*, 2008, **140**, 219.

49 G. A. Somorjai and J. Y. Park, *Catal. Lett.*, 2007, **115**, 87.